Breath Figures: Nucleation, Growth, Coalescence, and the Size Distribution of Droplets

Johannes Blaschke,[1,2] Tobias Lapp,[1,2] Björn Hof,[1] and Jürgen Vollmer[1,2]
[1]Max-Planck-Institut für Dynamik und Selbstorganisation (MPIDS), 37077 Göttingen, Germany
[2]Fakultät für Physik, Georg-August-Universität Göttingen, 37077 Göttingen, Germany
(Received 27 March 2012; published 10 August 2012)

The analysis of the size distribution of droplets condensing on a substrate (breath figures) is a test ground for scaling theories. Here, we show that a faithful description of these distributions must explicitly deal with the growth mechanisms of the droplets. This finding establishes a gateway connecting nucleation and growth of the smallest droplets on surfaces to gross features of the evolution of the droplet size distribution.

DOI: 10.1103/PhysRevLett.109.068701 PACS numbers: 68.43.Jk, 05.65.+b, 89.75.Da

Classical questions regarding breath figures involve the influence of material defects and impurities on the droplet patterns [1–5]. Presently, they are used as self-assembling templates in microfabrication [4,6–10] and as highly efficient means for heat exchange in cooling systems [5,11–13]. They are also promising candidates for water recovery in (semi-)arid regions [14,15]. For these applications, a detailed knowledge of the droplet size distribution and the average droplet growth speed is vital. Here, we demonstrate that the state of the art scaling theory [16–20] fails to describe data from simulations [21] and laboratory experiments [22], Fig. 1. A faithful description must, therefore, explicitly address the microscopic growth mechanisms of droplets.

Classical scaling [16,17] asserts that on clean surfaces the coagulation of droplets organizes the systems into a state where the number of droplets, $n(s, t)$, per unit droplet volume and surface area takes a universal scaling form,

$$n(s, t) = s^{-\theta} f\left(\frac{s}{S}\right), \quad \text{with } S = S(t). \tag{1a}$$

Here, s denotes the droplet volume, θ is a scaling exponent, $f(x)$ is a dimensionless function, and $S(t)$ is the volume of the largest droplets encountered at time t, i.e., the average volume of droplets in the *bump* of the distributions shown in Fig. 1.

Since $n(s, t)$ has a dimension of length to the power -5 the exponent θ must be set to a value of $\theta = 5/3$ [17–19]. The time evolution of $S(t)$ is found by observing that the total volume of all droplets grows linearly in time when a constant volume flux impinges onto the surface. In agreement with experimental and numerical observation [17–19], this entails $S(t) \sim t^3$. Moreover, a lower cutoff to the scaling at a scale s_0/S has been accounted for by a polydispersity exponent $0 < \tau < 2$ [23]. For our numerical scheme, where the mass flux onto the surface is implemented as sustained addition of droplets of size s_0 to random positions of the surface and where overlapping droplets are subsequently merged [22], it was predicted [20] to be

$$x \ll 1 \Rightarrow f(x) \sim x^{\theta-\tau}, \qquad \tau = 19/12. \tag{1b}$$

The scaling, Eq. (1a), provides an excellent data collapse of the *bump* and the *dip* of the numerical, Fig. 1(a), and the experimental data, Fig. 1(b). Beyond the *dip* one can discern a self-similar scaling regime, Eq. (1b), in the numerical data, and in only those experimental data with the vastest range of droplet sizes. On the other hand, in either case—and particularly pronounced in the experimental data—noticeable deviations, *tails*, from the scaling prediction arise for small values of s/S.

In the following, we show that these deviations result from features of droplet growth at the small length scale, s_0. Similar to the approaches in the theory of critical phenomena [24,25] or of the effect of rough boundaries in turbulent flows [26,27], scaling will be recovered by asymptotic analysis [28], which allows us to explicitly account for different growth mechanisms of small droplets. Universal and nonuniversal features of the asymptotic droplet density distribution will be disentangled by discussing the consequences of the different growth mechanisms for the small droplets in the numerical and experimental setting, respectively.

Relation to fractal packings.—To explore the role of the lower cutoff of scaling, we consider the droplet arrangement in breath figures as an example of a fractal packing of disks (see [29–31] for recent applications in other fields), and adopt scaling arguments developed to characterize (disordered) fractal structures to the problem at hand: We assert that in the scale-separation limit, $s_0 \ll S$, the free surface area, i.e., the area not covered by droplets, approaches a fractal with a fractal dimension $d_f < 2$. Self-similarity with fractal dimension d_f amounts, then, to the statement that in an area of size $S^{2/3}$ a number

$$N(s_*, S) \sim \left(\frac{S^{1/3}}{s_*^{1/3}}\right)^{d_f} = \left(\frac{s_*}{S}\right)^{-d_f/3} \tag{2}$$

of regions of size $s_*^{2/3}$ are required to cover the complement of the surface area covered by all droplets larger than s_*.

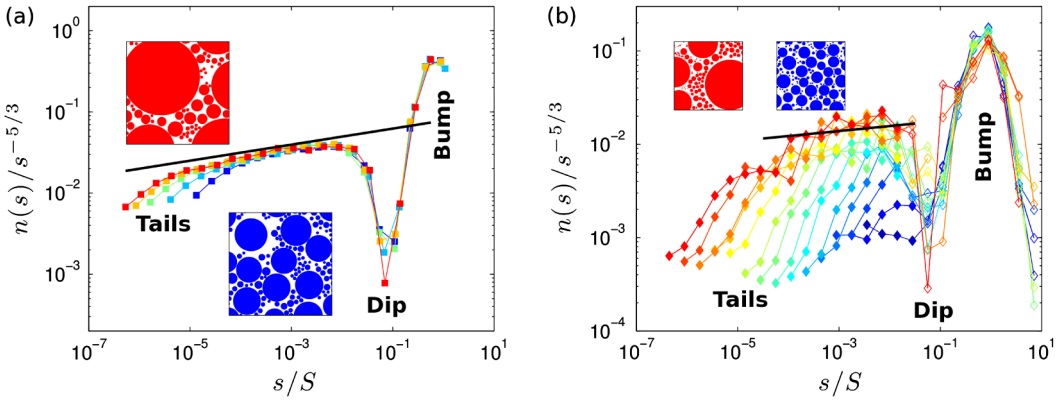

FIG. 1 (color online). Scaling plots of the droplet number density $n(s, t)$ for (a) numerical and (b) experimental data, for (a) 8×10^6 (rightmost *tails*), 12×10^6, 16×10^6, 20×10^6, and 24×10^6 (leftmost *tails*) droplets added to a domain of size 1600×1600 [22], and (b) water droplets on a polyethylene film [21] where eventually the droplet diameters cover the range from a few microns to a few millimeters. The respective positions of the *tail*, *dip*, and *bump* of the distributions are indicated, and the slope, $\theta - \tau = 1/12$, of the scaling prediction, [Eq. (1b)], is shown by solid lines. The insets show snapshots of the breath figures at an early [blue, (lower) right] and a late [red, left] time, respectively. Movies of their time evolution and full details of data assimilation and evaluation, as well as plots of the raw data are given in the Supplemental Material [22].

The fraction of this area in the considered domain of size $S^{2/3}$ amounts to

$$p(s_*, S) = N(s_*, S)\frac{s_*^{2/3}}{S^{2/3}} \sim \left(\frac{s_*}{S}\right)^{(2-d_f)/3}. \tag{3}$$

Following [29], we denote the surface area not covered by droplets as *porosity*, $p(t)$. It is obtained by evaluating Eq. (3) for the size s_0 characterizing the small-scale cutoff of the fractal, $p(t) = p(s_0, S(t))$.

By its definition the porosity is related the area A_d covered by droplets in a region of area A_s via $p(t) = 1 - A_d/A_s$: when the surface area in between droplets approaches a fractal of zero measure one obtains

$$\int_{s_0}^{\infty} a(s)n(s, t)ds \equiv \frac{A_d}{A_s} = 1 - p(t) \xrightarrow{s_0/S \to 0} 1,$$

where $a(s)$ denotes the area covered by droplets of size s. Using Eq. (1a) with $\theta = 5/3$, Eq. (1b), $a(s) \sim s^{2/3}$, and introducing $x = s/S$ one obtains

$$p(t) = 1 - \frac{A_d}{A_s} \sim \int_0^{s_0/S} x^{-1} f(x)\, dx \sim \int_0^{s_0/S} x^{\theta-\tau-1} dx = \left(\frac{s_0}{S(t)}\right)^{\theta-\tau}, \tag{4}$$

and comparing Eqs. (4) and (3) yields

$$\theta - \tau = (2 - d_f)/3. \tag{5}$$

Hence, the nontrivial scaling, Eq. (1b), of $f(x)$ for small x reflects the fractality of the arrangements of droplets in breath figures with a large scale separation $s_0 \ll S$, that can faithfully be regarded as a fractal.

This provides an independent, more accurate means to test the polydispersity exponent: For $\tau = 19/12$ and $S \sim t^3$, Eq. (4) implies $p(t) \sim t^{-1/4}$. Remarkably, none of our data follow this prediction [Figs. 1(b) and 5(b) in the Supplemental Material [22]]. Rather than 1/4, we find 0.30 for the numerical and 0.16 for the experimental data.

Hence, the different microphysics of droplet growth and merging leads to (slightly) different fractal dimensions and a different small-scale cutoff of scaling. To disentangle the intermediate self-similar scaling regime from the large scale (arising from the first generation of droplets, cf. [32]) and the small-scale physics, we introduce cutoff functions $\hat{f}(s/S)$ and $\hat{g}(s/s_0)$ for large and small droplets, respectively. $\hat{f}(x) \equiv f(x)/x^{\theta-\tau}$ takes a constant value $\hat{f}_0$ for $x \ll 1$, and it accounts for the *dip* and the *bump* in $n(s, t)$ for $s \simeq S$. Similarly, $\hat{g}(s/s_0)$ accounts for the *tails* of $n(s, t)$. As shown in the insets of Fig. 2, it approaches constant values for $s \gg s_0$, and it takes a scaling form for all times. To arrive at a complete description of the droplet size distribution, we further discuss this lower cutoff.

Incorporating the lower cutoff.—We start by writing the total volume of droplets of size s per unit volume ds and unit surface area in the form

$$s\, n(s, t) = S^{-2/3}\left(\frac{s}{S}\right)^{-d_f/3} \hat{f}(s/S)\, \hat{g}(s/s_0). \tag{6}$$

This expression states that in the scaling regime $s_0 \ll s \ll S$ the overall volume of droplets of size s on an area of size $S^{2/3}$ is proportional to the number of droplets, Eq. (2), of the considered size.

In equation (6) the fractal dimension d_f and the function $\hat{g}(s/s_0)$ are *not* universal. We, henceforth, adopt the values for d_f determined by fitting the porosity, and we follow the evolution of droplets smaller than s_* over a small time interval from t to $t + dt$ in order to relate the form of

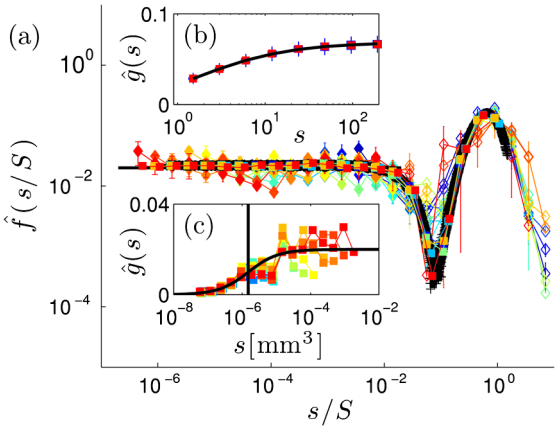

FIG. 2 (color online). Master plot of the universal cutoff function, $\hat{f}(s/S)$, which comprises all numerical and experimental data shown in Fig. 1 (using the same symbols), as well as additional numerical data shown as black crosses (every 5×10^4 frames of 44 runs where 4.23×10^7 droplets are added eventually). The insets show $\hat{g}(s)$ for (b) numerical and (c) experimental data at all times. Their shapes (solid lines) reflect the respective small-scale droplet growth mechanisms, Eqs. (10) and (11). The vertical line in (c) marks s_0.

$\hat{g}(s/s_0)$ to different nucleation and growth mechanisms of small droplets. Let the considered area on the substrate and the time interval dt be chosen such that this growth is not influenced by the merging of droplets larger than s_*. When s_* is so small that $\hat{f}(s_*/S)$ takes the constant value $\hat{f}_0$, Eq. (6) entails

$$s_* \, n(s_*, t) = \hat{f}_0 \, S^{-2/3} \left(\frac{s_*}{S}\right)^{-d_f/3} \hat{g}(s_*/s_0).$$

In order to determine $\hat{g}(s_*/s_0)$ we observe that the volume density of the droplets smaller than s_* amounts to the cumulative distribution

$$V(s_*) = \int_{s_0}^{s_*} s n(s,t) ds = \frac{\hat{f}_0}{S^{2/3}} \int_{s_0}^{s_*} \left(\frac{s}{S}\right)^{-d_f/3} \hat{g}(s/s_0) ds. \quad (7)$$

For values of s_* in the scaling regime the increase of volume is accounted for by increasing the integral domain. Therefore, an infinitesimal increase of s_* to $s_* + \dot{s}\, dt$ in the time interval dt amounts to an increase of the volume density of droplets,

$$\frac{dV}{dt} = \frac{V(s_* + \dot{s} dt) - V(s_*)}{dt} = \frac{\hat{f}_0}{S^{2/3}} \left(\frac{s_*}{S}\right)^{-d_f/3} \hat{g}(s_*/s_0) \, \dot{s}. \quad (8a)$$

On the other hand, this change must be due to the volume flux Φ onto the fraction of area covered by droplets,

$$\frac{dV}{dt} = p(s_*, S)\Phi \sim \left(\frac{s_*}{S}\right)^{(2-d_f)/3} \Phi. \quad (8b)$$

Equating the expressions for dV/dt, Eqs. (8a) and (8b), and dropping the subscript $*$, one obtains

$$\hat{g}(s/s_0) \sim \frac{\Phi}{\hat{f}_0} \frac{s^{2/3}}{\dot{s}}. \quad (9)$$

This expression provides the desired connection of the average speed $\dot{s}$ of the growth of droplets of size s to the form of the small-scale cutoff $\hat{g}(s/s_0)$ of $n(s, t)$: it explains how different microscopic droplet growth laws give rise to different nonuniversal cutoff functions $\hat{g}(s/s_0)$, and how the universal scaling is recovered for $s \gg s_0$. After all, the volume growth of large droplets in breath figures is always proportional to the area exposed to the surface flux [16,17,20], $\dot{s} \sim \Phi s^{2/3}$. Equation (9) allows us to disentangle universal and nonuniversal contributions to $n(s, t)$. This major finding of our theoretical treatment is now substantiated by working out the multiscaling predictions for the data shown in Fig. 1.

Scaling numerical data.—When a small droplet, of size s_0, has been added to the surface, it is merged with a droplet on the surface when the droplets overlap. As a consequence, a droplet of radius $s^{1/3}$ will capture small droplets of radius $s_0^{1/3}$, that are added in a distance smaller than $s^{1/3} + s_0^{1/3}$ from its center. In the absence of other droplets, this growth amounts to

$$\dot{s} \simeq \Phi\left[s^{1/3} + s_0^{1/3}\right]^2 = \Phi s^{2/3}\left[1 + \left(\frac{s_0}{s}\right)^{1/3}\right]^2.$$

The term in square brackets accounts for an enhanced growth of small droplets $s \gtrsim s_0$, which ceases rapidly for increasing s. In practice, the decay is even faster since the capture regions of neighboring droplets overlap. To fit the simulation data, Fig. 2(b), one needs a nontrivial prefactor 0.76 and an exponent close to 0.78 rather than 1/3,

$$\hat{g}(s/s_0) \simeq 0.07\left[1 + 0.76\left(\frac{s_0}{s}\right)^{0.78}\right]^{-2}. \quad (10)$$

Using Eq. (6) and $\theta - \tau = 0.3$ this provides a perfect data collapse of all numerical data, Fig. 2(a).

Scaling experimental data.—In the experimental setting, the growth rate of the droplets has two contributions. For small droplets, growth is limited by the diffusion of water molecules on the substrate towards the contact line of the droplet. As derived in [33] and observed in the experiments of [32], the radius of small droplets grows then like $r \sim t^{1/4}$, such that $\dot{s} \sim \Phi s^{-1/3}$. For larger droplets, the volume flux from the vapor phase onto the droplets is again proportional to the exposed droplet surface, such that $\dot{s} \sim \Phi s^{2/3}$. These growth contributions combine to

$$\dot{s} \sim \Phi s^{2/3}\left(1 + \frac{s_0}{s}\right) \Rightarrow \hat{g}(s/s_0) = b\left(1 + \frac{s_0}{s}\right)^{-1}, \quad (11)$$

where $s_0 \simeq 1.5 \times 10^{-6}$ mm^3 is the crossover size scale and $b \simeq 2 \times 10^{-2}$ is a normalization constant. Inserting Eq. (11) into Eq. (9) provides an excellent prediction for $\hat{g}(s/s_0)$, Fig. 2(c). Also, for the experimentally measured droplet size distributions, one obtains a perfect data collapse of the

appropriately scaled droplet number density $n(s, t)$ for all different times, Fig. 2(a).

Discussion.—For the numerical data, s_0 amounts to the volume of the smallest droplets in the system, Fig. 2(b), and for the experimental data it is about one order of magnitude larger than the smallest observed droplets, Fig. 2(c). In either case $\hat{g}(s)$ saturates for $s \gtrsim 10^2 s_0$. On the other hand the scaling behavior Eq. (1b) is only accessible for values of s below the *dip* of the distribution, i.e., for $s \lesssim 10^{-2}$ S. It can, hence, only be resolved in simulations where $10^{-4} \ll s_0/S$, resulting in the observed scaling regime of about 1–2 decades, in the numerical data, Fig. 1(a), and in the experimental data with the largest accessible scale separation, Fig. 1(b).

Because of the relatively small scaling range, the droplet size distribution of breath figures cannot merely be idealized as a self-similar process with a single relevant length scale $S(t)$ [16–19]. Rather, one explicitly has to cope with the growth law of the smallest droplets in the system. Via its (slight) effect on the fractal dimension characterizing the free space in between the droplets, Eq. (5), it sets the value of the polydispersity exponent τ, and it leads to massively different cutoff functions $\hat{g}(s/s_0)$, Figs. 2(b) and 2(c), that can completely dominate the shape of the droplet size distribution, Fig. 1(b).

When both the large scale and the small scale cutoffs are properly accounted for via Eqs. (10) and (11), a remarkable data collapse of all experimental *and* numerical data into a single plot is achieved, Fig. 2(a). This recovery of scaling establishes a novel gateway connecting features of the microscopic droplet growth on surfaces to gross features of the evolution of the droplet size distribution.

We are grateful to Bruno Eckhardt, Jens Eggers, Franziska Glaßmeier, Walter Goldburg, Siegfried Großmann, Andrew Scullion, and Stephan Herminghaus for enlightening discussions, and to our referee for very valuable feedback on the manuscript.

[1] Rayleigh, Nature (London) **86**, 416 (1911); J. Aitken, *ibid.* **90**, 619 (1913).
[2] T. J. Baker, Philos. Mag. Ser. 6 **44**, 752 (1922).
[3] G. P. Lopez, H. A. Biebuyck, C. D. Frisbie, and G. M. Whitesides, Science **260**, 647 (1993).
[4] J. Lepopoldes and P. Damman, Nature Mater. **5**, 957 (2006).
[5] B. S. Sikarwar, N. K. Battoo, S. Khandekar, and K. Muralidhar, J. Heat Transfer **133**, 021501 (2011).
[6] A. Böker *et al.*, Nature Mater. **3**, 302 (2004).
[7] M. Haupt, S. Miller, R. Sauer, K. Thonke, A. Mourran, and M. Moeller, J. Appl. Phys. **96**, 3065 (2004).
[8] Y. Wang, A. S. Özcan, C. Sanborn, K. F. Ludwig, and A. Bhattacharyya, J. Appl. Phys. **102**, 073522 (2007).
[9] K. Rykaczewski, J. Chinn, M. L. Walker, J. H. J. Scott, A. Chinn, and W. Jones, ACS Nano **5**, 9746 (2011).
[10] A. Z. Samuel, S. Umapathy, and S. Ramakrishnan, ACS Appl. Mater. Interfaces **3**, 3293 (2011).
[11] M. Mei, B. Yu, M. Zou, and L. Luo, Int. J. Heat Mass Transfer **54**, 2004 (2011).
[12] R. N. Leach, F. Stevens, S. C. Langford, and J. T. Dickinson, Langmuir **22**, 8864 (2006).
[13] J. W. Rose and L. R. Glicksman, Int. J. Heat Mass Transfer **16**, 411 (1973).
[14] I. Lekouch, M. Muselli, B. Kabbachi, J. Ouazzani, I. Melnytchouk-Milimouk, and D. Beysens, Energy **36**, 2257 (2011).
[15] V. Nikolayev, D. Beysens, A. Gioda, I. Milimouka, E. Katiushin, and J.-P. Morel, J. Hydrol. **182**, 19 (1996).
[16] D. Beysens, A. Steyer, P. Guenoun, D. Fritter, and C. Knobler, Phase Transit. **31**, 219 (1991).
[17] P. Meakin, Rep. Prog. Phys. **55**, 157 (1992).
[18] J. L. Viovy, D. Beysens, and C. M. Knobler, Phys. Rev. A **37**, 4965 (1988).
[19] F. Family and P. Meakin, Phys. Rev. A **40**, 3836 (1989).
[20] J. A. Blackman and S. Brochard, Phys. Rev. Lett. **84**, 4409 (2000).
[21] Droplet patterns are obtained from water droplets suspended from a polyethylene film covering a glass plate kept at a temperature of 20 °C which is placed about 5 cm atop a water bath with a temperature of 60 °C. See Supplemental Material at http://link.aps.org/supplemental/10.1103/PhysRevLett.109.068701 for details on the experimental method as well as raw data and a movie of the evolution.
[22] See Supplemental Material at http://link.aps.org/supplemental/10.1103/PhysRevLett.109.068701 for full details on the numerical method as well as raw data and a movie of the evolution.
[23] S. Cueille and C. Sire, Phys. Rev. E **55**, 5465 (1997).
[24] L. P. Kadanoff, W. Götze, D. Hamblen, R. Hecht, E. A. S. Lewis, V. V. Palciauskas, M. Rayl, J. Swift, D. Aspnes, and J. Kane, Rev. Mod. Phys. **39**, 395 (1967).
[25] R. Hilfer, Phys. Rev. Lett. **68**, 190 (1992).
[26] G. I. Barenblatt and A. J. Chorin, Proc. Natl. Acad. Sci. U.S.A. **101**, 15 023 (2004).
[27] N. Goldenfeld, Phys. Rev. Lett. **96**, 044503 (2006).
[28] G. I. Barenblatt, *Scaling* (Cambridge University Press, New York, 2003).
[29] H. J. Herrmann, G. Mantica, and D. Bessis, Phys. Rev. Lett. **65**, 3223 (1990); S. S. Manna and H. J. Herrmann, J. Phys. A **24**, L481 (1991); S. D. S. Reis, N. A. M. Araújo, J. S. Andrade, Jr., and H. J. Herrmann, Europhys. Lett. **97**, 18004 (2012).
[30] A. Amirjanov and K. Sobolev, Model. Simul. Mater. Sci. Eng. **14**, 789 (2006).
[31] F. Varratoa and G. Foffia, Mol. Phys. **109**, 2663 (2011).
[32] D. Fritter, C. M. Knobler, and D. A. Beysens, Phys. Rev. A **43**, 2858 (1991).
[33] T. M. Rogers, K. R. Elder, and R. C. Desai, Phys. Rev. A **38**, 5303 (1988).